A Cellulose Encapsulated Composite Electrolyte Design: Towards Chemically and Mechanically Enhanced Solid-sodium Batteries

Shu Dong,[1] Geng Xie,[1] Shihong Xu,[2] Xuehai Tan,[2] Madhusudan Chaudhary,[1] Yue Zhang,[4] Runqi Wu,[1] Fuwei Wen,[1] Cagri Ayranci,[3] Vladimir K. Michaelis,[1] Amanda Quirk,[5] Scott M. Rosendahl,[5] Jian Liu,[4] Michael Fleischauer,[6,7] Lingzi Sang[1,4]*

[1]Department of Chemistry, [2]nanoFAB Fabrication and Characterization Facility, [3]Department of Mechanical Engineering, [7]Department of Physics, University of Alberta, Edmonton, Alberta, Canada T6G 2G2

[4]School of Engineering, Faculty of Applied Science, University of British Columbia, Kelowna, British Columbia, Canada, V1V 1V7

[5]Canadian Light Source, 44 Innovation Boulevard, Saskatoon, Saskatchewan, Canada, S7N 2V3

[6]National Research Council Nanotechnology Research Centre, 11421 Saskatchewan Dr NW, Edmonton, T6G 2M9

*Corresponding Author: Lingzi Sang, lsang@ualberta.ca

Abstract

Replacing liquid electrolytes with solid ionic conductors attracts increasing attention due to the potential of improved battery safety. Solid-state batteries show potential for further increased energy/power density by eliminating the use of packaging accessories for unit cells. Sulfide- and halide-based ceramic ionic conductors exhibit comparable ionic conductivity with liquid electrolytes. These materials, however, are inherently brittle, making them unfavorable for applications. Here, we report a mechanically enhanced composite Na^+ conductor that contains 92.5 wt% of sodium thioantimonate (Na_3SbS_4, NSS) and 7.5 wt% of sodium carboxymethylcellulose (CMC); the latter serves as the binder and an electrochemically inert encapsulation layer. The ceramic and binder constituents were integrated at the particle level, providing ceramic NSS-level Na^+ conductivity in the NSS-CMC composite, the more than five-fold decrease of electrolyte thickness obtained in NSS-CMC composite electrolytes provided a five-fold increase in Na^+ conductance compared to NSS ceramic pellets. Resulting from the CMC encapsulation, this NSS-CMC composite shows increased moisture resistivity and electrochemical stability, which significantly promotes the cycling performance of NSS-

based solid-state batteries, and improves ductility of the material. This work demonstrates a well-controlled, orthogonal process of ceramic-rich, composite electrolyte processing – independent streams for ceramic particle formation along and binder encapsulation in a solvent-assisted environment. This work provides insights into the interplay among the solvent, the polymeric binder, and the ceramic particles in composite electrolyte synthesis, and implies the critical importance of identifying the appropriate solvent/binder system for the precise control of this complicated process. Finally, the work also provides valuable insights into the potential of designing mechanically tailorable battery components via fundamental understanding of the effect of the constituents on the overall composite ductility.

TOC figure

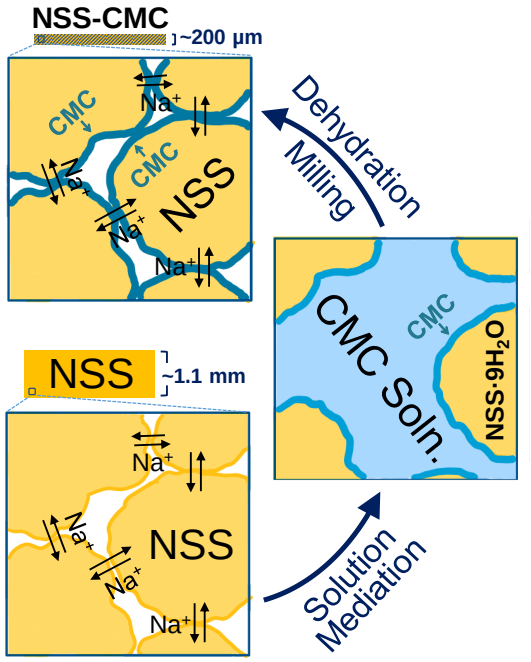

1. Introduction

All-solid-state sodium batteries are safe and sustainable alternatives to liquid-electrolyte lithium-based batteries and they pave the way for a cost-effective grid-scale energy storage. Ceramic Na^+ conductors exhibit relatively high room-temperature ionic conductivity and a wide electrochemical stability window,[1] however, this class of material shows limited ductility, and thus producing thin and bendable electrolytes for compact, high-energy/power density cells is particularly challenging. Polymer electrolytes exhibit enhanced mechanical properties, yet suffer from relatively low room-temperature Na^+ conductivity, low transference number (for dual-ion electrolytes), and limited electrochemical stability window.[2-5] The ionic conductivity of polymer electrolytes depends strongly on the glass transition temperature of the polymer matrix, which defines the optimal temperature for polymer chain relaxation to access reasonable ion mobility. Although single-ion polymer electrolytes designed for unity transference numbers have been reported,[6-8] their electrochemical stability still needs to be improved.

Composites comprised of ceramic and polymer constituents can potentially combine the advantage of mechanical ductility and high ionic conductivity.[9] Previous work shows that there are two possible ion transport pathways in a given composite electrolyte, the ceramic and the polymer constituent.[10-12] In either case, the constituent responsible for ion transport must exceed the ion percolation threshold.[10-12] Ion exchange across the ceramic and polymer interface was found to require substantial activation energy and this process is usually correlated with decomposition chemistry.[10, 13, 14] In polymer-rich composites, low weight-percentage oxide ceramic electrolytes were introduced and functioned as plasticizers.[15-17] In these systems, low conductivity and limited stability remain an issue. Recent work shows that it is feasible to fabricate ceramic-rich composites as Na^+ and Li^+ conductors,[18-22] although ceramic-rich Na-composites are not as well understood as Li-composites. For example, Ren and coworkers demonstrated a cross-linking sodium thioantimonate (NSS) -polymer electrolyte, enabling the fabrication of solution-casted electrolyte membranes.[23] A low Na^+ resistance (65 $\Omega \cdot cm^{-2}$) was demonstrated in an ultra-thin electrolyte membrane.

However, composite electrolytes obtained using this approach only contain ≤50 mol% of NSS, which is likely limits the Na^+ percolation in the NSS constituent of the composite. The cross-linked NSS plausibly adopts a different fundamental Na^+ transport mechanism compared to ceramic NSS, limiting the overall conductivity. In another example, a new halide Li^+ conductor LiCl-GaF_3 was discovered to show clay-like pliable properties, despite the unresolved decomposition chemistry when the material is in contact with metallic lithium.[24] Beyond the effort on discovering structurally modified solid-electrolytes, Wang and co-workers introduced low-concentration binders (0.5 wt% of polytetrafluoroethylene, PTFE) into Li_6PS_5Cl, Li_3InCl_6, and $Li_{6.5}La_3Zr_{1.5}Ta_{0.5}O_{12}$ via shear mixing to produce thin membranes. The woven-like PTFE binder supported the structural integrity of the membrane.[21] This method realized ceramic-rich composites containing ultra-low polymer loading and bypassed the challenge of selecting compatible solvents for the integration of ceramic and polymer. The shear mixing process can be energy-intensive, and it is less practical to accommodate large-scale processing under the required inert environments.

Herein, we report a NSS-based ceramic-rich composite electrolyte comprised of 92.5 wt% of NSS, and 7.5 wt% of sodium carboxymethylcellulose (CMC). This composite was fabricated using a solution-assisted approach and water is used as the mediating solvent. A ~50 nm CMC encapsulation layer formed on the NSS particle surface provided enhanced ductility to the material, enabling the production of free-standing pellets. While a Na^+ conductivity of 0.4 $mS \cdot cm^{-1}$ was obtained in NSS-CMC compared to 1.0 $mS \cdot cm^{-1}$ in NSS, as a result of enhanced ductility, the reduced electrolyte thickness provided more than doubled area conductance in NSS-CMC compared to NSS. High conductance is required to realize the optimal cell kinetics and energy density by minimizing overall electrolyte impedance. CMC encapsulation also introduces a physical barrier to enhance the stability of NSS when interacting with moisture or experiencing reducing conditions near metallic sodium electrodes. Through a rigorous characterization of this NSS-CMC composite, we demonstrate the feasibility of designing solvent-assisted approaches to control the formation of ceramic-rich electrolyte composites.

2. Results and Discussion

2.1 Composition, structure, and Na^+ conductivity

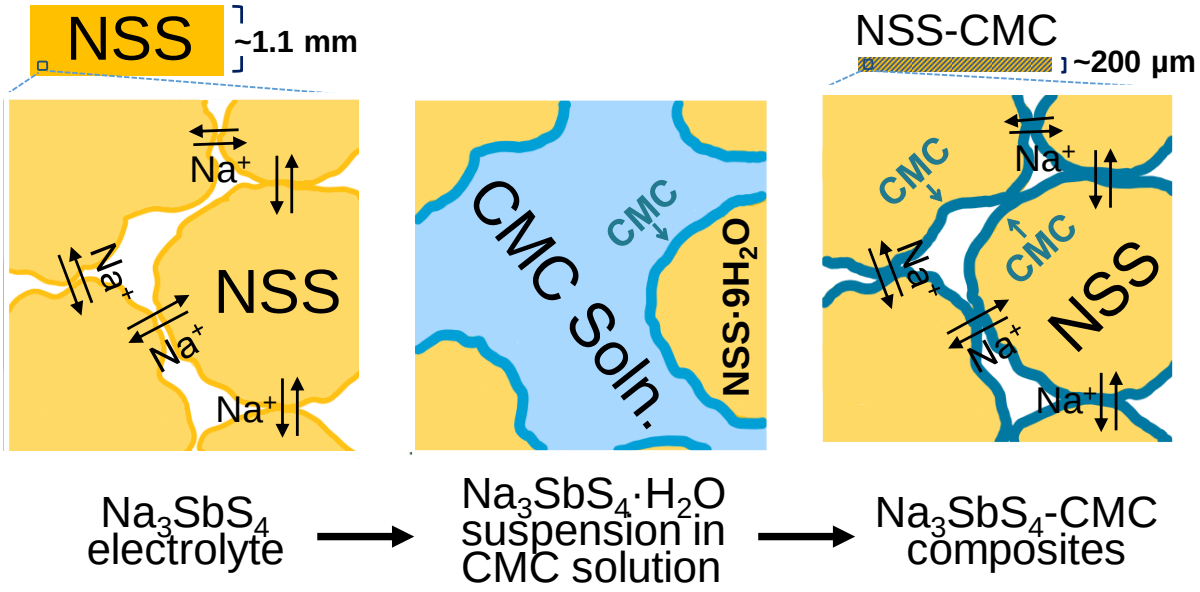

Scheme 1. Formation of NSS-CMC composites

Scheme 1 illustrates the formation of NSS-CMC composites by solution processing. Specifically, a CMC coating forms on the surface of hydrated NSS particles in a CMC/H_2O solution. This coating is solid after re-dehydration. A post-ball milling process further reduces the particle size to access the increased Na^+ conductivity. Qualitatively, we obtained NSS-CMC composite electrolyte pellets as thin as 100 μm – less than 10% of the thickness compared to a ceramic NSS pellet, showing a more flexible and ductile overall structure that is likely due to the effect of the CMC interfaces formed between NSS particles. Further tailoring of the mechanical properties can be achieved by controlling the CMC thickness and/or NSS particle size, i.e., an increased relative thickness of the CMC interface will enhance the ductility and flexibility of the structure. Details on the mechanical properties and the determining factors at the composite structural level are beyond the scope of this study and will be reported in upcoming publications.

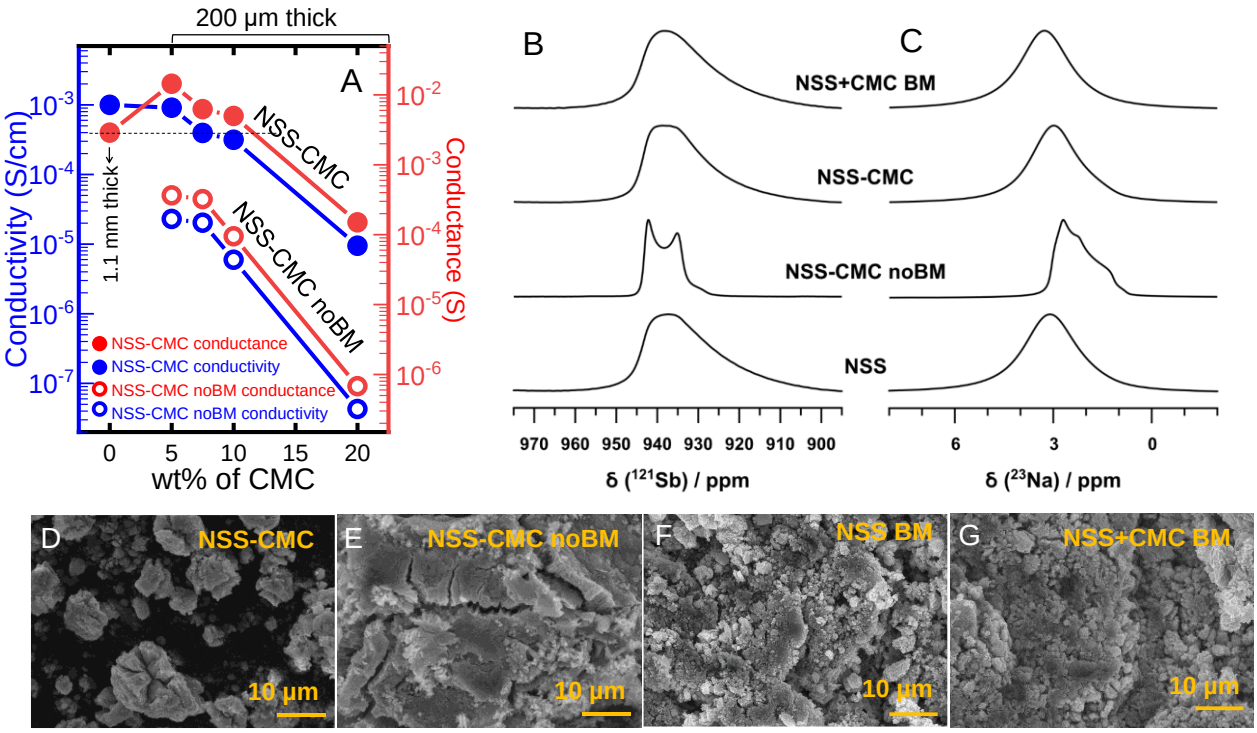

Figure 1. *(A) Conductivity and Conductance of NSS-CMC (solid circle) and NSS-CMC noBM (open circle). (B) ^{121}Sb and (C) ^{23}Na solid-state NMR spectra (B_0 = 18.8 T, ν_r = 10 kHz) for NSS and its various synthetically modified composites. SEM images obtained from powder samples (D) NSS-CMC, (E) NSS-CMC noBM, (F) NSS BM, and (G) NSS+CMC BM.*

Fig. 1A shows the Na^+ conductivity of NSS-CMC composites containing 0 – 20 wt% of CMC. To minimize the mechanical inconsistency across all samples, this work uses a 200 µm thick electrolyte for characterizations. The first addition of 10 wt% CMC induced a slight decrease in room-temperature Na^+ conductivity from 1.0 mS·cm^{-1} to 0.5 mS·cm^{-1} and when 20 wt% of CMC was introduced a more significant decrease in Na^+ conductivity to 0.08 mS·cm^{-1} was observed. However, the reduced electrolyte thickness results in high area conductance in the NSS-CMC composite. Specifically, composites containing 5 wt% CMC show 15 mS of area conductance, which is five times higher compared to the NSS pellets with no CMC incorporation, and 10 wt% CMC addition provides approximately doubled area conductance compared to a NSS pellet. We determined that the addition of 7.5 wt% CMC can simultaneously provide a high area conductance and sufficient mechanical strength to maintain a thin pellet structure.

Therefore, 7.5 wt% CMC was chosen to conduct further characterization and electrochemical performance studies.

Na^+ conductivity and the electrolyte pellet performance are highly dependent on the processing approach. Dry mixing is insufficient to result in particle-level integration and a visually consistent pellet morphology is not achieved. Although NSS-CMC obtained after the solution process and re-dehydration shows visually homogeneous morphology, the enhanced Na^+ conductivity was not accessed until a post ball milling process was conducted. Shown in **Fig. 1A,** NSS-CMC pre- and post-ball milling exhibit a marked difference in Na^+ conductivity: NSS-CMC pre-ball milling (annotated as NSS-CMC noBM in figures) show approximately 2 orders of magnitude lower Na^+ conductivity compared to the ball milled composites (annotated as NSS-CMC in figures). This contrast is consistent across all composite samples containing 5-20 wt% of CMC, although a similar trend of Na^+ conductivity decreasing as CMC content increased is observed for conductivity measurements pre- and post-ball milling. We note that mechanochemical processes can potentially alter the structure, crystal phases, and morphology of ceramic Na^+ conductors, resulting in unexpected changes to structure, particle size, crystallinity, and morphology of the material, which in consequence alters its intrinsic ionic conductivity.[25]

We further interrogated the structure of NSS when the material undergoes solution mediation process with the CMC binder. To understand the correlation between the structure of NSS-CMC composites and its conductivity, we characterized the NSS crystal structure, Sb-S polymorph, and the local chemical environment of Na and Sb within NSS. Raman spectra obtained from NSS and NSS-CMC both show the signature symmetric (v_s near 362 cm^{-1}) and asymmetric stretch (v_{as} near 385 cm^{-1} and 405 cm^{-1}) of SbS_4 tetrahedron, indicating that the tetrahedral SbS_4 structure was retained after the introduction of CMC (**Fig. S1A**). NSS and pre-ball milled NSS-CMC show similar diffraction patterns, indicating the crystal structure of NSS remained after solution processing. After ball milling, diffraction peak broadening was observed across the entire 2θ range, indicating a reduced crystallinity in NSS-CMC. (**Fig. S1B**)

The local chemical structure of the NSS-CMC composite was accessed via solid-state ^{121}Sb and ^{23}Na NMR performed at 18.8 T. The ^{121}Sb MAS NMR (**Fig. 1B**) of NSS revealed a greater distribution of electric field gradients (EFG) at the local Sb chemical environments, as expected from a less crystalline material due to mechanochemical treatment.[26] When NSS is mixed with CMC in water followed by dehydration to produce pre-ball milled NSS-CMC (NSS-CMC noBM), long-range crystallinity is introduced back, consistent with the distinct ^{121}Sb second order quadrupolar lineshape, demonstrating the asymmetric SbS_4^{3-} tetrahedron which experiences non-zero EFG consistent with the tetragonal structure of Na_3SbS_4.[27] In dry mixed NSS+CMC, a similar ^{121}Sb NMR spectrum is observed due to a Czjzek distribution onset by the distribution of the EFG about Sb Chemical environments. The collective ^{121}Sb NMR spectra suggest that mechanochemical treatment in NSS-CMC decreases the crystallinity by onset of local and medium-range disorder, however, the asymmetrical local site symmetry in SbS_4^{3-} tetrahedron is retained in the tetragonal system ($P\bar{4}2_1c$), as a symmetrical ^{121}Sb lineshape is expected only when Sb experiences a zero EFG (i.e., cubic Na_3SbS_4 ($I\bar{4}3m$)).[28, 29] Although, studies in the analogue compound, Na_3PS_4, have shown that mechanochemical treatment can introduce discrepancy between local and long-range structures,[30] our complimentary PXRD, Raman, and NMR analyses confirm that the crystallinity (sharpness of the diffraction peaks) decreases in NSS-CMC post mechanochemical treatment but retains the tetragonal crystalline symmetry.[31]

Similar results are observed for the ^{23}Na MAS NMR data in **Fig 1C**, whereby a unique quadrupolar lineshape was observed in ^{23}Na NMR spectrum of NSS-CMC pre-ball milling (NSS-CMC noBM), consistent with two sodium environments experiencing motion as demonstrated in its analogue Na_3PS_4 tetragonal phase.[32] As crystallinity decreases, the distinctive quadrupolar lineshape smooths and broadens due to the distribution in EFG and reduction in long-range order introduced through mechanochemical treatments. In such materials, ^{23}Na quadrupolar lineshapes are further influenced by Na^+ dynamics and magnetic field strengths, inhibiting the two Na crystallographic sites to be resolved.[32] Finally, the NMR resonances do not interfere with those from the CMC sodium salt – the ^{23}Na NMR peak for CMC (pre- and post-ball milling) appears at a lower chemical shift and is reduced in intensity due to the low concentration of composite (**Fig. S2**) used here.

We attempted to determine possible oxidation state change in CMC using XPS. Although CMC pre- and post-ball milling show similar C 1s and O 1s spectra, suggesting CMC likely retains its unchanged through mechanochemical treatment, (**Fig. S3**) due to the low CMC concentration, the oxidation state change of CMC in NSS-CMC composite was not accessible. (**Fig. S4**)

The morphology of NSS composite particles is shown in **Fig. 1D**. Prior to ball milling the composites are aggregated solids. (**Fig. 1E**) After ball milling, the NSS-CMC appear distinctly different as scattered particles ranging from 1 – 10 µm in diameter. Pristine NSS appears as clustered micron-size particles (**Fig. 1F**) similar to the morphology of NSS+CMC prepared by dry ball-milling (**Fig. 1G**) and aggregates were not observed in either sample. This result indicates that adding CMC facilitates the formation of aggregates that were milled down to micron-size NSS-CMC particles (High-magnification images are shown in **Fig. S5**.). Indeed, pristine CMC shows a smoother morphology, and its electrical insulating property induces intense backscattered electrons in the SEM images (**Fig. S5I)**. Ball milling CMC induces no significant effects on its morphology (**Fig. S5J**). The fact that neither CMC-containing composites (**Fig. 1B** and **1C**) nor the NSS+CMC dry mixture (**Fig. 1E**) show apparent CMC content in the EM images suggests that the 7.5 wt% CMC is likely incorporated into NSS particles. This particle-level integration results in a unique aggregate-like morphology in pre-ball milled NSS-CMC, which converts to the smaller and dispersed particles in the NSS-CMC composites post-ball milling. This dispersion plausibly reduces the stress concentration levels in the composite, leading to reduced premature failures and, consequently, increased ductility in the material.

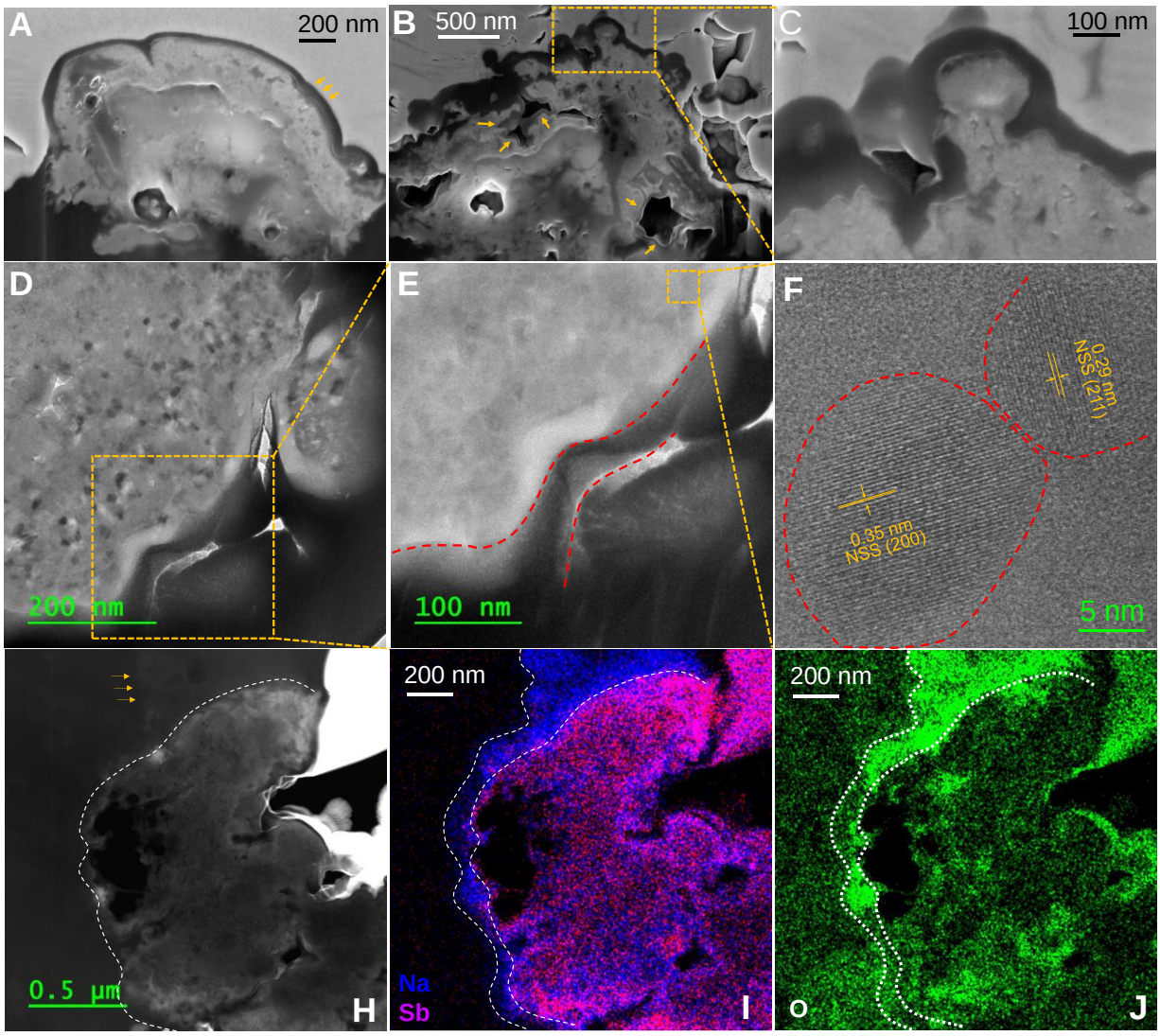

Figure 2. *CMC coating on NSS particles. (A-C) SEM images showing NSS particles coated with ~50 nm of CMC layers, (D-F) TEM and HRTEM showing the detailed structure of the CMC coating and the NSS crystal lattice inside the polycrystalline particle, (H-J) TEM-EDX showing the elemental composition of the coated NSS-CMC particle*

The NSS-CMC particles were examined by electron microscopy. **Fig. 2A – 2C** shows SEM images of a lamella cross-sectioned from a NSS-CMC particle. We observed a continuous coating layer covering the surface of the ceramic particle. This layer is approximately 50 nm thick and exhibits morphology and conductivity distinctly different from the inside of the particle. This thin coating layer covers the surface of voids inside the particle in addition to the coating appearing at the outermost particle surface (by

gold arrows shown in **Fig. 2B**). Coatings were also observed in TEM images acquired at the edge of a particle (**Fig. 2D** and **2E**). The inside of the ceramic particle is polycrystalline in nature as indicated by the two distinct crystal lattice planes, NSS (2 0 0) and (2 1 1) (**Fig. S6**), observed in the HRTEM shown in **Fig. 2F**; and no direct evidence of coating layer presence in between different crystal phases within the polycrystalline particle was obtained. The distribution of Na, Sb, (**Fig. 2H**), and O (**Fig. 2J**) were acquired from a particle lamella shown in **Fig. 2H**. Inside the particle shows a homogeneous distribution of Na and Sb, suggesting the presence of NSS. In contrast, at the edges of the particle, Sb is absent, and Na appears, which is consistent with the presence of a Na-containing layer, attributed to the CMC Na salt. Inside the particle near the edges of voids, slightly more pronounced Na signals appear, although occupying a significantly thinner layer inside the voids. This observation suggests the presence of a thin coating on the surface of voids within a polycrystalline particle. An enhanced O signal near the edges of the particle (**Fig. 2J**) was observed and is consistent with the oxygen-containing CMC layer. The non-zero oxygen signal inside the particle is likely due to unavoidable air contamination when the lamella is transferred between the FIB-SEM and the TEM chambers. Collectively, the combination of electron microscopy and the energy dispersion X-ray analysis provided an insightful picture of the CMC-coated polycrystalline NSS particle. This H_2O-mediated solution processing enabled the dissolved CMC to form a ~50 nm-thick, morphologically continuous encapsulation layer on the surface of undissolved, hydrated NSS particles. This robust, continuous coating layer is maintained on the outer surface and voids of the particles upon NSS dehydration and ball milling after solution processing.

2.2 Moisture and Electrochemical Stability

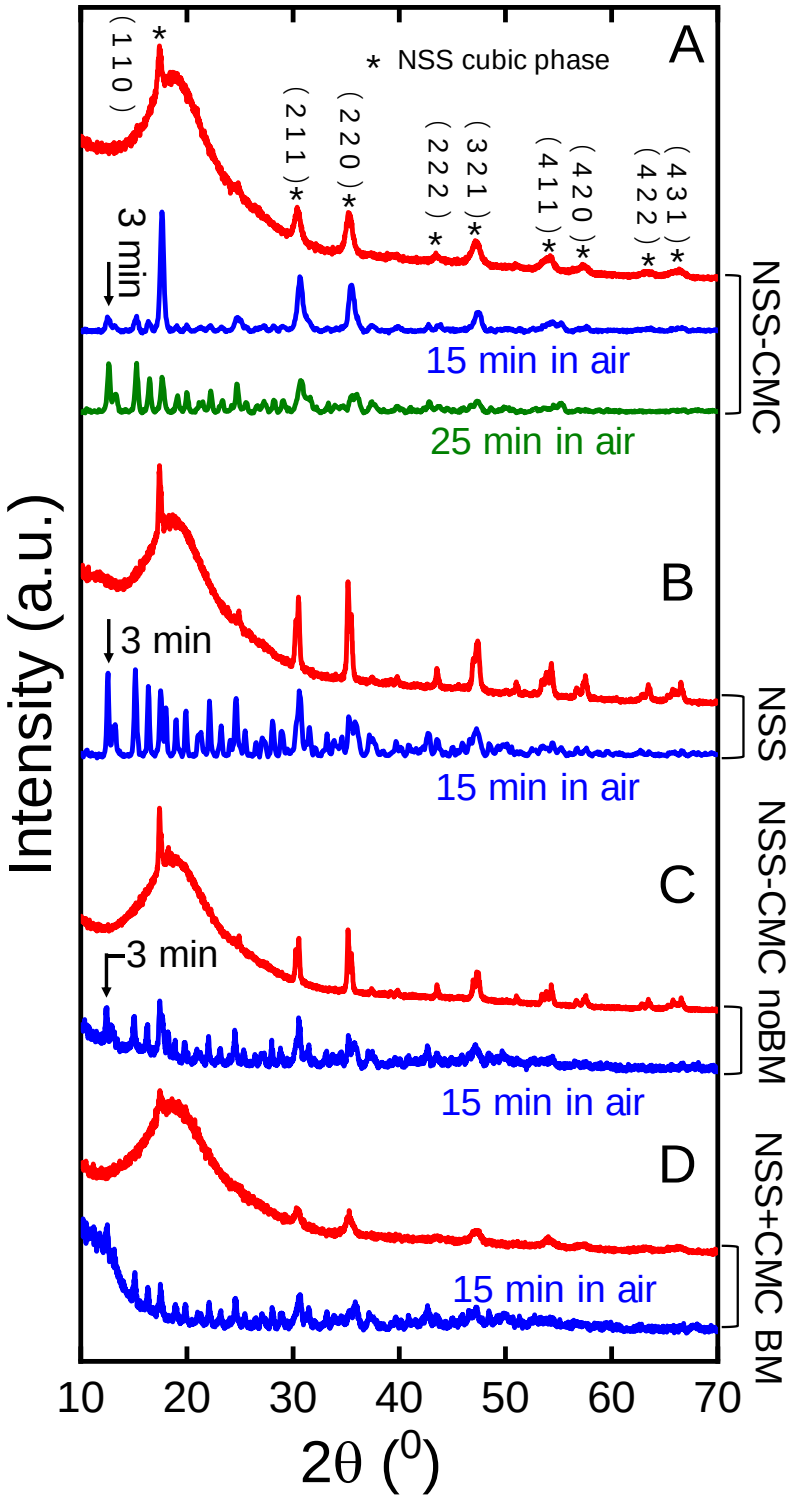

2.3

Figure 3. *Moisture resistivity of NSS composites: Powder XRD obtained from (A) NSS-CMC, (B) NSS, (C) NSS-CMC noBM, and (D) NSS+CMC ball-milled mixture before and after air exposure.*

In **Fig. 3** we compare the PXRD pattern of NSS-containing samples before and after air exposure. As seen in **Fig. 3A**, NSS-CMC maintains its diffraction pattern after at least 15-min air exposure. After 25 min of air exposure, NSS-CMC shows a similar PXRD as the hydrated NSS ($Na_3SbS_4 \cdot 9H_2O$).[33] In contrast, this hydrated form of NSS was observed in pristine NSS that experienced 15 min air exposure. (**Fig. 3B**) As the PXRD scan started almost simultaneously with NSS exposure to air, the first signature peak for hydrated NSS was captured within 3 min of NSS interaction with air, suggesting limited moisture resistivity of NSS. Interestingly, NSS-CMC pre-ball milling does not exhibit comparable moisture resistivity – the formation of hydrated NSS also appears within the first 3 min of air exposure. (**Fig. 3C**) This observation indicates that CMC film may form following the solution process, however, the CMC-encapsulated individual particles only emerge after post-ball milling. To further test the hypothesis of CMC encapsulation-induced moisture resistivity, we acquired the diffraction pattern of the dry ground mixture of NSS and CMC (NSS+CMC) with the equivalent duration of post ball milling after the solution process. As shown in **Fig. 3D**, similar moisture resistivity was not observed in the dry mixed NSS+CMC sample, suggesting no protective CMC encapsulation formed. Combined with the microscopy results, these observations suggest that the continuous coating on the outside of the particle plays a role in preventing moisture penetration into the NSS particle and thus suppresses the unwanted hydration process. The H_2O mediation likely assists the formation of CMC-coated NSS aggregates (**Fig. 1C**). These coated aggregates, however, are not sufficient to provide a functional moisture barrier. A post ball milling step is essential to create the CMC-encapsulation on individual NSS particles ranging from 1 – 20 μm in diameter; and the resulting ~50 nm CMC coating is responsible for the enhanced moisture resistivity seen in the NSS-CMC composites.

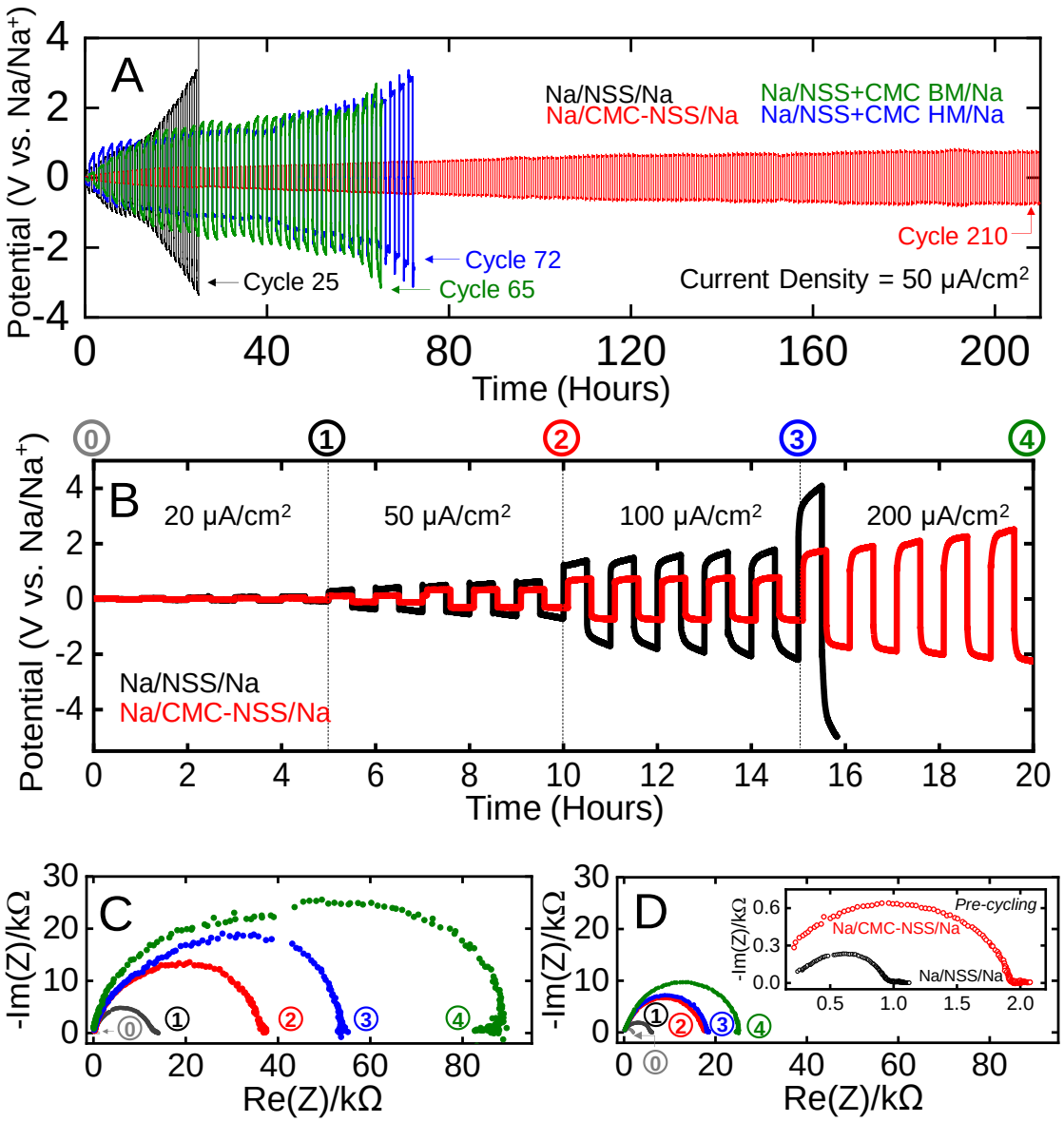

Figure 4. *Electrochemical Stability of NSS composites: (A) Comparisons of Galvanostatic charge/discharge behavior of Na/SE/Na symmetric cells at a current density of 50μA/cm² using NSS, NSS-CMC, NSS+CMC ball-milled or hand mixed electrolytes. (B) Rate performances of Na/NSS/Na cell compared to Na/NSS-CMC/Na cell, along with the EIS results obtained from (C) the Na/NSS/Na cell and (D) the Na/NSS-CMC/Na cell following the charge/discharge cycles at each current density.*

In **Fig. 4** the electrochemical cycling performance of Na/SE/Na symmetric cells using NSS-CMC composite electrolyte is examined. As shown in **Fig. 4A**, the Na/NSS/Na cell experienced a dramatic increase in its overpotential (to 3.1 V vs. Na/Na^+) within the first 25 cycles when operated at a 50 $\mu A/cm^2$ current density. This increased overpotential is

a result of NSS decomposition forming Na-ion blocking Na-Sb binary structures, SbS_3^{3-}, and $Sb_2S_7^{4-}$ dimers when contacting Na electrode and/or experiencing Na reduction potentials.[33] Cycled at the same current density, a Na/NSS-CMC/Na cell can operate over 210 cycles before its overpotential approaches 1.0 V (vs. Na/Na^+). The decreased overpotential seen in the Na/NSS-CMC/Na cell suggests the suppressed decomposition of NSS, consistent with a CMC coating that prevents the direct exposure of NSS to metallic Na or to function as a voltage barrier. The Na/NSS-CMC/Na cell also shows increased overpotential upon cycling, although the magnitude was significantly smaller compared to a Na/NSS/Na cell. Therefore, NSS decomposition is still present even with a CMC encapsulation layer in place. By way of contrast, the suppressed overpotential was not observed in cells containing dry mixed NSS and CMC (hand ground or ball milling). These observations are consistent with our hypothesis – a continuous CMC coating must be present on NSS particles for the enhanced electrochemical stability of NSS-CMC composites.

In **Fig. 4B** we compared the rate performance of a Na/NSS-CMC/Na versus a Na/NSS/Na cell. Operated at increased current densities (up to 200 $\mu A/cm^2$), 5 cycles at each current density step, the Na/NSS-CMC/Na cell shows relatively stable cycling performance with significantly lower overpotential at all steps, indicating the suppressed formation of Na^+ blocking materials as a result of decomposition. EIS measurements were performed at the end of each step, and a significantly larger overall cell impedance was observed in the Na/NSS/Na cell, although the impedance of the pre-cycled Na/NSS/Na cell was smaller compared to the pre-cycled Na/NSS-CMC/Na cell. (**Fig 4C and 4D**) The evolvement of the interfacial resistivity is quantified from the EIS results using an equivalent circuit as provided in **Table S1**. This result suggests that CMC coating on NSS slightly reduces the intrinsic Na^+ conductivity in the electrolyte, however, the coating provided an enhanced electrochemical stability for NSS-based electrolyte.

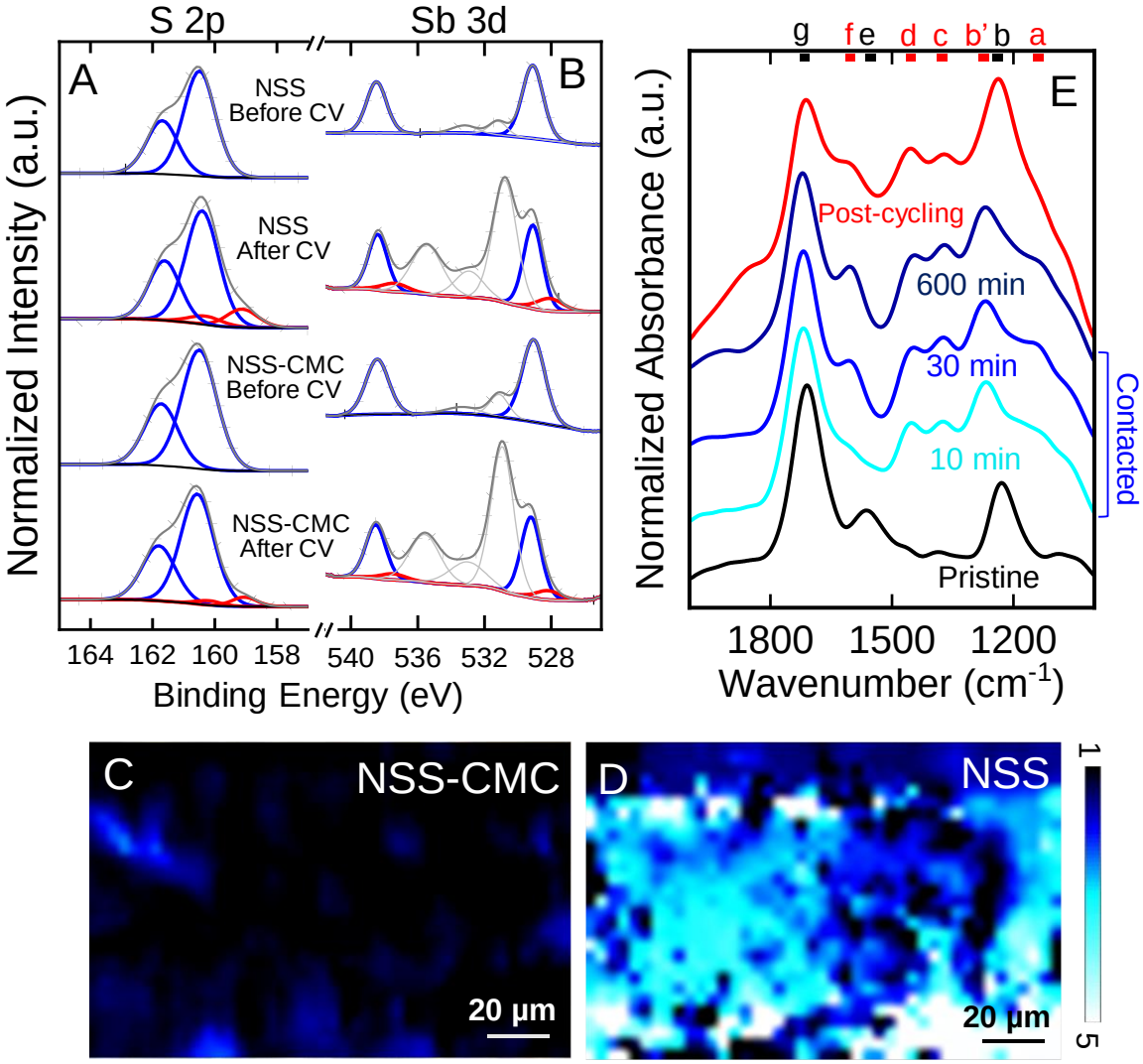

Figure 5. *Decomposition of NSS and its composites following charge/discharge cycles. (A) S 2p and (B) Sb 3d core-level XPS obtained from NSS and NSS-CMC before and after CV cycles; 2-dimensional Raman mapping obtained from (C) NSS and (D)NSS-CMC surface recovered from Na/SE/Na cells post CV cycles. (E) ATR-IR spectra obtained from the NSS-CMC composite electrolyte surface before and after contacting the Na electrode.*

To examine the electrochemical stability of NSS-CMC, electrolytes before and after electrochemical cycling were characterized. **Fig. 5A** and **5B** show the S 2p and Sb 3d XPS obtained from NSS and NSS-CMC composites before and after 10 charge/discharge cycles in Na/SE/Na cells at 50 μA/cm^2. In both electrolytes, lower binding energy S 2p and Sb 3d peaks were observed after cycling, suggesting the reduction of S and Sb to form Na_2S and Na-Sb binary.[33] The relative peak area of

reduced S and Sb components with respect to S and Sb in pre-cycled electrolytes was quantified. Specifically, we found 11.6 % of reduced S and 24.1% of reduced Sb in post-cycled NSS. By way of contrast, 6.8% of S and 12.2% of Sb were found reduced in NSS-CMC after cycling. (**Table S2**) We conducted 2D Raman mapping on electrolyte surfaces detached from Na electrodes after cycling to access the heterogeneity of this decomposition across the electrolyte surface. **Fig. 5C** and **5D** are heat maps of the relative intensity of the 140 cm^{-1} peak with respect to the peak near 362 cm^{-1}. The 140 cm^{-1} peak is the Na-Sb stretching mode associated with the Na-Sb binary phase, a signature decomposition product of NSS, and 362 cm^{-1} is the symmetric stretch of SbS_4, a featured peak in pristine NSS. In the Raman imaging, we observed a higher relative intensity and a wider distribution of the Na-Sb binary in the post-cycling NSS electrolyte compared to that of NSS-CMC. This result is consistent with the suppressed chemical reduction in NSS-CMC observed from XPS (**Fig. 5A** and **5B**). Collectively, CMC coating functions as a chemically stable barrier that inhibits the direct reduction of NSS when contacting metallic Na. We inquire whether CMC maintain its structure when preventing the reduction of NSS, or presumably in the harsh reducing condition during Na deposition and stripping, CMC would convert to a different structure – a passivating material that covers the NSS particle. To address this question, we interrogated the possible structural change in CMC when the composite is subjected to electrochemical reduction. **Fig. 5E** shows a series of ATR-FTIR spectra obtained from the surface of pristine NSS-CMC composites, NSS-CMC after contacting metallic Na for 10 min to 10 hours, and NSS-CMC recovered from a Na/SE/Na cell after cycling. As observed from the spectra, CMC present in the as-prepared NSS-CMC composite shows three major vibrational modes: **b** near 1236 cm^{-1}, **e** near 1550 cm^{-1}, and **g** at 1712 cm^{-1}. Specifically, peak **b** is associated with the stretch of –COH,[34-36] **g** results from the stretch of –C=O in –COOH,[35, 37] both reveal the presence of protonated CMC. Peak **e** was unidentified but was previously observed in protonated cellulose. Post-contacting Na or after CV cycles in a Na/NSS-CMC/Na cell, new peaks **f** (1602 cm^{-1}), **d** (1454 cm^{-1}), and **c** (1373 cm^{-1}) emerge, while peak **b** shifted to a slightly higher frequency near 1265 cm^{-1}. In addition, we observed the shoulder peak **a** near 1136 cm^{-1}. The new peaks **f** and **d** are attributed to the asymmetric and symmetric stretch of $–COO^-$ in deprotonated carboxylic acid

group.[35, 36] A similar peak **g** (ν(-C=O)) to **f** (ν_s(-COO^-)) and **d** (ν_{as}(-COO^-)) transition was observed in CMC solutions as a result of pH increase, inducing deprotonation of the carboxylic acid group. This phenomenon was also observed when carboxylic acids were converted to their sodium salts.[35-38] Although the exact assignment was not clear, peak **c** was observed in CMC under extreme basic conditions, which is likely associated with its deprotonation.[34, 39] Similarly, the frequency increase seen in peak **b** is likely a result of deprotonation of –COH upon reduction chemistry.[34-36] The new shoulder peak **a** near 1136 cm^{-1} was attributed to vibrational modes of the CMC backbone,[37, 40] and its change in frequency and intensity has been attributed to backbone rearrangement, likely resulting from CMC deprotonation. A complete peak assignment is provided in **Table S3**. Collectively, the ATR-FTIR results suggest that the CMC coating in general maintains its molecular structure while undergoing (electro) chemical reduction. And deprotonation of –COH and –COOH were observed along with CMC backbone rearrangement. The exact structure of the CMC coating and its optimization in structure, local pH, and thickness aiming for the most chemically resistive and ionically conductive are important topics that require further investigation.

2.3 Te-C/NSS-CMC/Na All-solid-state Cell

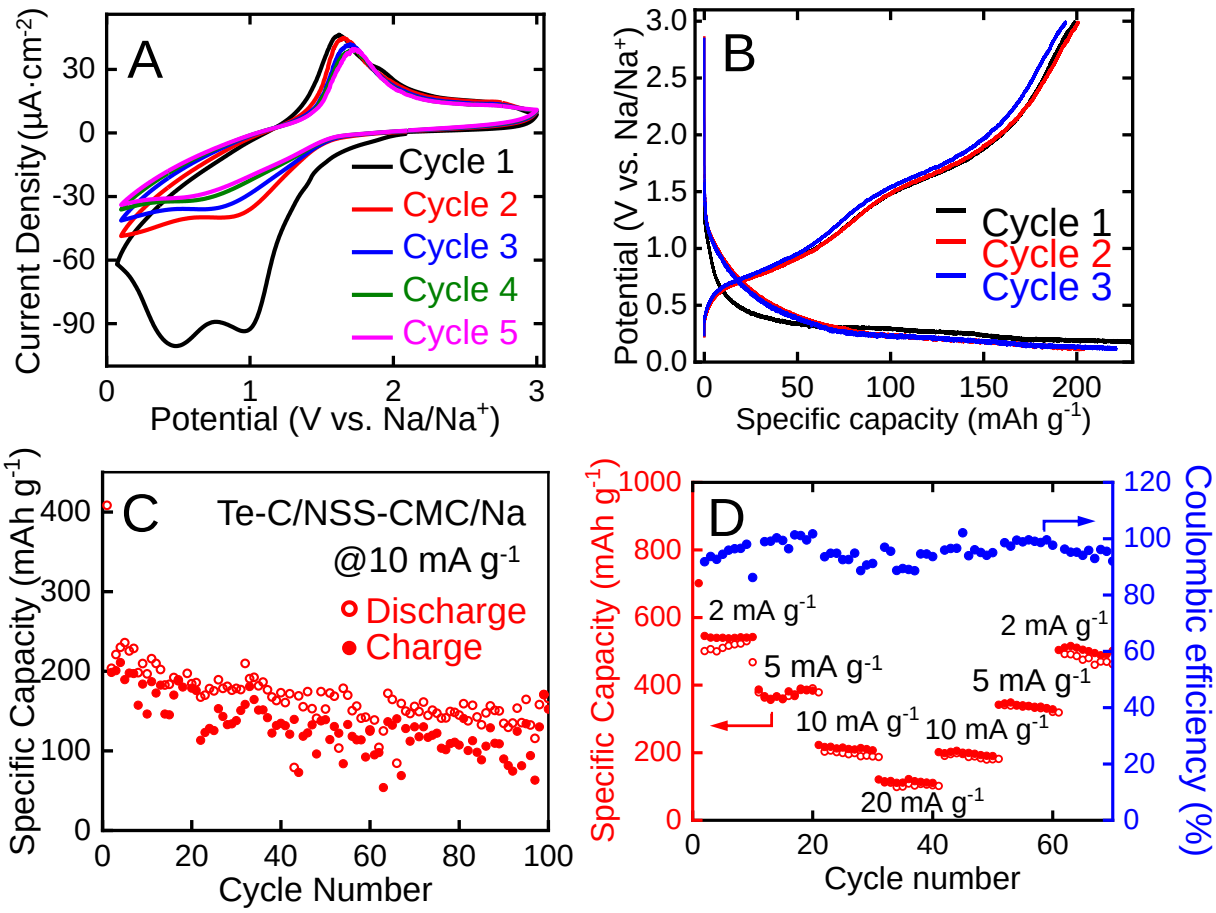

Figure 6. *Electrochemical performance of a Te-C/NSS-CMC/Na battery. (A) Cyclic Voltammetry obtained at a scan rate of 0.2 mV/Sec, (B) the first three galvanostatic charge/discharge cycles, (C) Specific capacity obtained from the cell charge/discharged at 10 mA·g-1, and (D) the rate performance and Coulombic* efficiency *of cells operated at different charge/discharge rates.*

The use of NSS-CMC composite electrolyte was demonstrated in a Te-C/NSS-CMC/Na cell. The Te-C electrode is chosen as a conversion electrode for this solid sodium battery. Previous work showed that Te-C converts to Te-metal alloy when Li^+ and K^+ undergo redox chemistry, where the microporous carbon acted as a host for Te-Li and Te-K insertion/desertion to support the structural stability and to provide stable storage capacity by accommodating volume expansion and preventing Te dissolution.[41] Na^+ storage has also been reported in Te-C electrodes, likely exhibiting similar reaction mechanism.[42] **Fig 6A** shows the first five cycles of the cyclic voltammetry obtained from

a Te-C/NSS-CMC/Na cell. Relatively stable redox peaks were observed starting cycle 2, despite a slight observable current density decrease. The drastic current density decrease seen in cycle 2 compared to the first CV cycle is due to an irreversible formation of the electrode/electrolyte interface. In **Fig. 6B**, we demonstrated the galvanostatic charge/discharge cycles between 0.2 and 3.0 V (vs. Na/Na^+) at a current density of 10 mA/g. A charge/discharge capacity at ~ 150 mAh·g was obtained in the first 100 cycles. (**Fig. 6C**) In particular, we observed specific capacities of 545, 386, 224, and 121 mAh·g when operating at current densities of 2, 5, 10, and 20 mA/g respectively. (**Fig. 6D**) Although substantially lower charge/discharge current was employed due to the slow kinetics in solid-state battery systems in general when compared to liquid cells, the capacity of 545 mAh/g obtained at 2 mA/g charge/discharge current is comparable to the maximum accessible capacity observed in liquid cell systems using Te-C electrodes.[41-44] This Te-C/NSS-CMC/Na cell also shows reasonably stable charge/discharge performance when operating at a step-wise decreased current density following measurements at increased rates. Specific capacities of 201, 341, and 503 mAh/g were obtained at 10, 5, and 2 mA/g respectively. Quantitatively 88%-92% of the specific capacity was accessed compared to charge/discharge cycles at the initially decreased current density steps. Coulombic efficiencies are maintained between 89% to 100% throughout the rate performance evaluation. These results demonstrated the application of NSS-CMC composite electrolytes in conversion-type electrodes.

3. Conclusion

This work reported a cellulose-encapsulated NSS composite electrolyte for high-energy-density solid-state sodium batteries. The ~50 nm thick CMC encapsulation accounts for only <0.5% of the NSS particle diameter, yet the mechanically enhanced interface CMC offered has promoted the ductility of NSS, enabling the fabrication of ~ 100 µm thick electrolyte pellets, <10% of the thickness of a pristine NSS ceramic pellet. This ultra-thin CMC encapsulation slightly impedes the intrinsic Na^+ mobility within the material, however, the reduced electrolyte thickness provided higher Na^+ conductance in NSS-CMC compared to the pristine NSS, compensated for its reduced Na^+ conductivity. The

NSS-CMC composite shows promoted cycling performance in symmetric cells. We also demonstrated its application when integrated into a full-cell configuration that uses a Te-C conversion electrode. Characterization results suggest that the CMC coating layer provides a physical barrier to separate NSS from metallic Na electrodes and moistures in the environment. The CMC coating also creates a voltage barrier to prevent the direct exposure of NSS to extreme potentials. During electrochemical cycling, the CMC coating maintains largely stable with minor transitions from its protonated to deprotonated structure along with backbone rearrangement.

In this work, we demonstrated a solution-processing strategy that enabled a well-controlled formation of a polymer coating on ceramic electrolyte particles. The properties ultimately dictate the ionic conductivity and mechanical ductility of a composite electrolytes include particle size and encapsulation layer thickness. These properties are potentially tunable with the choice of solvent and polymer system. This work implies that the selection of solvent-polymer-ceramic system is of critical importance for the precise control of the two orthogonal processes – the recovery of ceramic particles with the desired structure and morphology, and the formation of coatings at the thickness of choice. We highlight the demand for a systematic understanding of chemistries among ceramic electrolyte particles, processing solvents, and polymer binder candidates – the principle that underpins the optimal processing approach for a chemically and mechanically enhanced composite electrolyte.

4. Methods

Preparation of Na_3SbS_4-sodium carboxymethyl cellulose composite (NSS-CMC).

The starting materials sodium carboxymethyl cellulose (powder), elemental S (powder, 99.998%), anhydrous Na_2S (powder, 98%), Sb_2S_3 (powder, 99.995%) were all obtained from MilliporeSigma, and were used as received. Na_3SbS_4 (NSS) were synthesized using a water-mediated approach.[33, 45] Specifically, Na_2S, Sb_2S_3 and S powders at the stoichiometric ratio were mixed in water to form $Na_3SbS_4 \cdot 9H_2O$, which was further purified by recrystallization. The resulting $Na_3SbS_4 \cdot 9H_2O$ was then reground and dehydrated at 200 ℃ under vacuum to obtain the anhydrous Na_3SbS_4. The anhydrous

Na_3SbS_4 was then ball-milled for 1 hour to produce the as-prepared Na_3SbS_4 (NSS) electrolyte.

To synthesize the NSS-CMC composite, 50 mg of CMC was first dissolved in milli-Q water to form a 2.5 wt% CMC solution. The solution was stirred for 3 hours to achieve complete dissolution. Subsequently, NSS powders were added to the CMC solution to synthesize the desired composition of the NSS-CMC composite. For the targeted 5 wt%, 7.5 wt%, 10 wt%, and 20 wt% of CMC in the final composite, 950.0, 616.7, 450.0, and 200.0 mg of NSS were introduced. The resulting mixtures were stirred for 3 hours to achieve a homogeneous dispersion before being transferred to a vacuum oven to dehydrate at 120°C for 24 hours. The resulting powders were then ball milled for 1 hour to produce NSS-CMC. To understand the structure of NSS-CMC, composite electrolyte containing 7.5 wt% of CMC before ball mill (NSS-CMC noBM) and the dry mixed NSS and CMC at the same weight ratio by either 10 min hand grinding (NSS+CMC HG) or 1-hour ball milling (NSS+CMC BM) were also prepared for characterizations.

Preparation of Te-C electrode

Porous carbon substrate was purchased from Adven Industries Inc. and was used as received. Metallic Te (99.99%) was obtained from Fenix Advanced Materials. Te-carbon (Te-C) composites were prepared via a melting-diffusion method.[41-44, 46] Specifically, solid Te powders and porous carbon were mixed at a 2:1 mass ratio and calcined in a quartz tube for 6 h at 550 ℃ (i.e.,100 ℃ above the melting temperature of Te). The calcination process was protected under continuous nitrogen flow (99.999%). The weight percentage of Te within the Te-C composite was measured to be 49% via thermogravimetric analysis (TGA). (**Fig. S7**)

Electrochemical Characterizations

All the electrochemical impedance (EIS), cyclic voltammetry (CV), and charge/discharge cycles of Na/CSE/Na symmetric cells were performed on a Bio-Logic SP200 potentiostat. The charge/discharge cycling and rate performance measurements of Te-C/NSS-CMC/Na cells were conducted on a LANDE M310A battery test system.

For the electrochemical measurements, the pellets of NSS, NSS-CMC noBM, NSS+CMC HG, and NSS+CMC BM were prepared by compressing ~80 mg of materials at 1.5 tons in an ¼ inch diameter die set. The resulting pellets were ~ 1.1 mm in thickness. NSS-CMC pellets were compressed under the same condition using 30 mg of material, and the resulting pellet was ~200 µm. ~100 µm thick NSS-CMC pellets were obtained by compressing 20 mg of materials under the same condition. Na/SE/Na cells were assembled by placing freshly cut metallic Na pellet on each side of the electrolyte pellet prior to analysis. For the preparation of Te-C/NSS-CMC/Na cells, Te-C cathode powder was ball mill mixed with NSS-CMC electrolyte at a 2:1 Te-C to NSS-CMC mass ratio. This composite cathode powder was then pressed onto a 100 µm thick NSS-CMC pellet at 1.5 tons. This double-layered pellet was then attached to a freshly cut Na chip to produce a Te-C/NSS-CMC/Na full cell.

The intrinsic Na^+ conductivity of electrolyte materials was measured using a C/SE/C cell configuration. EIS were performed in a 7MHz to 0.01 Hz frequency range. CV measurements obtained from the Na/SE/Na symmetric cell were conducted by scanning the voltage of one Na electrode between -0.2V and 0.2V (vs. Na/Na^+) at a rate of 0.2 mV/sec. Galvanostatic charge and discharge cycles were performed on Na/CSE/Na symmetric cells at various current output and were all kept at 60 min per cycle. CV of the Te-C/NSS-CMC/Na cell was conducted between a voltage window of 0.1V – 3V (vs. Na/Na^+) at a scan rate of 0.2 mV/sec, and the galvanostatic charge and discharge cycles were performed at various constant current between 0.1 V to 3.0 V.

Powder X-ray Diffraction (PXRD) was obtained from a Bruker D8 X-ray diffractometer. Cu Kα line (λ=1.5418 Å) is used as the radiation source, sample diffraction was scanned between 5-90° at a step rate of 5°/min. To prevent air exposure, samples are sealed under a Kapton tape during the analysis.

Raman characterizations were obtained from a Renishaw inVia confocal Raman microscope. 532 nm excitation was used. Raman scattering between 110 and 1136 cm^{-1} was acquired using a 50X objective lens. Spectra were a result of 60 accumulative scans. The two-dimensional Raman imaging was measured within a 100 µm × 150 µm region.

X-ray photoelectron spectroscopy measurements were conducted on a PHI 5000 Versa Probe III spectrometer. Monochromatic Al Kα was used as the X-ray source. The base pressure of the analysis chamber was kept at 3.8×10^{-10} torr during the analysis. Au $4f_{7/2}$ peak at 84.0 eV was used to calibrate each spectrum. A pass energy of 280 eV was used when acquiring the survey scans, and a 55 eV pass energy was used to acquire high-resolution spectra. Spectra analysis and quantifications were performed using CasaXPS software. Peak fittings were conducted using combined Gaussian and Lorentzian functions. Marquardt algorithm was used to determine the optimal peak model parameters.

Scanning electron microscopy (SEM) images were acquired using a HITACHI-4800 field emission high-resolution SEM. An accelerating voltage of 15.0 kV was used at a SE (M) detector. The base pressure of the analysis chamber was kept at 1.3×10^{-6} torr throughout the analysis. Samples were protected under Ar when transferring from the glovebox to the SEM chamber. To access the constituents of the NSS-CMC particle, cross-section milling was performed on a ThermoFisher Helios Hydra Plasma FIB and SEM dual beam system to obtain a sample lamella for the analysis. Specifically, a 30 kV Xe beam was used for milling the cross-section. Prior to milling, carbon, and tungsten were deposited on the surface of the sample to protect the sample from damage by Xe ion beam impinging. The obtained cross-section was further polished using Xe beam operated at 30 kV and 1 nA, 30 kV and 30 pA, and at 5 kV and 100 pA sequentially. STEM/EDX analysis was performed on a JEOL JEM ARM200cf S/TEM system equipped with a cold field emission gun and Cs probe corrector. EDX maps were obtained using a 100 mm 2 JEOL SDD detector.

^{121}Sb and ^{23}Na NMR data were acquired on a Bruker Avance NEO 800 (B_0 = 18.8 T) NMR spectrometer using a 4 mm double-resonance (H/X) Bruker magic-angle spinning (MAS) probe. Powdered samples were mixed with dry silica (50 % by weight) and packed into 4 mm (outer diameter) ZrO_2 rotors with Kel-F drive caps inside an argon glovebox. The ^{121}Sb NMR data were acquired under MAS conditions (ν_r = 10 kHz) using a Bloch decay pulse sequence with a short tip angle of 0.4 μs (ν_{rf} = 62.5 kHz, liquid), a recycle delay of 0.01 s and 20480 co-added transients. The ^{121}Sb NMR spectra were referenced to 0 ppm using solid $KSbF_6$ (ν_r = 14 kHz). The ^{23}Na NMR data were acquired under MAS conditions

(v_r = 10 kHz) using a Bloch decay pulse sequence with a short tip angle of 0.6 μs (v_{rf} = 42 kHz, liquid), a recycle delay of 0.1 s and 1024-5120 co-added transients. The ^{23}Na NMR spectra were referenced to 0.1 M NaCl solution (0 ppm).

The *attenuated total reflection infrared spectra (ATR-IR)* were acquired at a horizontal attenuated total reflection (h-ATR) microscope at the mid-infrared beamline at the Canadian Light Source. The endstation of this instrumentation has been described previously.[47-49] Briefly, this endstation is a conjugate focus microscope where an off-axis parabolic mirror (OAP) focuses the incident beam onto the sample and a second OAP collects the reflected light to direct it toward the detection leg of the endstation. The optics are initially aligned based on external reflection from a gold mirror at the sample focus and both the Internal reflection element (IRE) sample position and the downstream collection optics are be repositioned to account for the change in the focal position introduced by the IRE refractive index. A focal plane array (FPA) infrared detector with 64 × 64 pixels at 3-fold magnification is used for macro-ATR imaging using a globar source. Spectra were collected with 256 coadded interferograms and 4 cm^{-1} resolution. The experiments described use a ZnSe face angle crystal (FAC) at 45° as the IRE and a home built electrochemical cell design. By using the FPA detector, a focused field of view of approximately 500x500um was possible and heterogeneities in the surface could be tracked.

Supporting Information

Raman, NMR, XPS spectra, and SEM images obtained from NSS and NSS-CMC at different stages of solution processing; Thermo gravimetric analysis results of the Te-C electrode; EIS quantification results; XPS S_{2p} and Sb_{3d} quantification results; HATR peak assignment for pristine NSS-CMC, and NSS-CMC post contacting Na or post cycling.

Author Information

Corresponding Author

*Lingzi Sang, lsang@ualberta.ca

Author Contributions

The manuscript was written with the contribution of all authors. All authors have approved the final version of the manuscript. S.D., G.X., and L.S. conducted the composite electrolyte synthesis, optimization, and electrochemical characterization; S.X. and X.T. performed FIB-SEM-TEM analysis; M.C. and V.K.M. conducted NMR analysis; Y.Z. and J.L. contributed to Te-C full cell fabrication; R.W., C.A., and M.F. contributed to mechanical analysis; S.D., RW., A.Q., and S.R. contributed to HATR characterization.

Notes

The authors declare no competing financial interest.

Acknowledgments

L.S. is supported by the Natural Sciences and Engineering Research Council (NSERC) of Canada Discovery program, the Alberta Innovates – NSERC Alliance Advance program, the Canada Foundation for Innovation, and the Government of Alberta. L.S. and M.F. are supported by the National Research Council Canada, New Beginnings program. V.K.M. acknowledges support from the Canada Research Chairs program (CRC-2020-00352) and the Chemistry Centre for Magnetic Resonance (C^2MR) Facility, which is funded by the Canada Foundation for Innovation (CFI), the Government of Alberta, and the Faculty of Science. J.L. is supported by the NSERC Discovery program (RGPIN-2023-03655), Mitacs, Canada Foundation for Innovation (CFI), British Columbia Knowledge Development Fund (BCKDF), and UBC Eminence Program.

Reference

1. Liu, G.; Yang, J.; Wu, J.; Peng, Z.; Yao, X., Inorganic Sodium Solid Electrolytes: Structure Design, Interface Engineering and Application. *Adv. Mater.* **2024**, 2311475.
2. Chen, S.; Che, H.; Feng, F.; Liao, J.; Wang, H.; Yin, Y.; Ma, Z.-F., Poly(vinylene carbonate)-Based Composite Polymer Electrolyte with Enhanced Interfacial Stability To Realize High-Performance Room-Temperature Solid-State Sodium Batteries. *ACS Appl. Mater. Interface* **2019,** *11* (46), 43056-43065.
3. Elbinger, L.; Enke, M.; Ziegenbalg, N.; Brendel, J. C.; Schubert, U. S., Beyond Lithium-ion Batteries: Recent Developments in Polymer-based Electrolytes for Alternative Metal-ion Batteries. *Energy Storage Mater.* **2024,** *65*, 103063.
4. Fall, B.; Prakash, P.; Gau, M. R.; Wunder, S. L.; Venkatnathan, A.; Zdilla, M. J., Experimental and Theoretical Investigation of the Ion Conduction Mechanism of

Tris(adiponitrile)perchloratosodium, a Self-Binding, Melt-Castable Crystalline Sodium Electrolyte. *Chem. Mater.* **2019,** *31* (21), 8850-8863.
5. Yang, J.; Zhang, H.; Zhou, Q.; Qu, H.; Dong, T.; Zhang, M.; Tang, B.; Zhang, J.; Cui, G., Safety-Enhanced Polymer Electrolytes for Sodium Batteries: Recent Progress and Perspectives. *ACS Appl. Mater. Interface* **2019,** *11* (19), 17109-17127.
6. Zhang, H.; Li, C.; Piszcz, M.; Coya, E.; Rojo, T.; Rodriguez-Martinez, L. M.; Armand, M.; Zhou, Z., Single Lithium-ion Conducting Solid Polymer Electrolytes: Advances and Perspectives. *Chem. Soc. Rev.* **2017,** *46* (3), 797-815.
7. Liu, K.; Xie, Y.; Yang, Z.; Kim, H.-K.; Dzwiniel, T. L.; Yang, J.; Xiong, H.; Liao, C., Design of a Single-Ion Conducting Polymer Electrolyte for Sodium-Ion Batteries. *J. Electrochem. Soc.* **2021,** *168* (12), 120543.
8. Dong, X.; Liu, X.; Li, H.; Passerini, S.; Bresser, D., Single-Ion Conducting Polymer Electrolyte for Superior Sodium-Metal Batteries. *Angew. Chem. Int. Ed.* **2023,** *62* (43), e202308699.
9. Maurya, D. K.; Dhanusuraman, R.; Guo, Z.; Angaiah, S., Composite polymer electrolytes: progress, challenges, and future outlook for sodium-ion batteries. *Adv. Compos. Hybrid Mater.* **2022,** *5* (4), 2651-2674.
10. Popovic, J.; Brandell, D.; Ohno, S.; Hatzell, K. B.; Zheng, J.; Hu, Y.-Y., Polymer-based hybrid battery electrolytes: theoretical insights, recent advances and challenges. *J. Mater. Chem. A* **2021,** *9* (10), 6050-6069.
11. Sen, S.; Trevisanello, E.; Niemöller, E.; Shi, B.-X.; Simon, F. J.; Richter, F. H., The Role of Polymers in Lithium Solid-state Batteries with Inorganic Solid Electrolytes. *J. Mater. Chem. A* **2021,** *9* (35), 18701-18732.
12. Zhang, Z.; Chen, H.; Hu, Z.; Zhou, S.; Zhang, L.; Luo, J., Ion Conduction Path in Composite Solid Electrolytes for Lithium Metal Batteries: from Polymer Rich to Ceramic Rich. *Front. Energy* **2022,** *16* (5), 706-733.
13. Busche, M. R.; Drossel, T.; Leichtweiss, T.; Weber, D. A.; Falk, M.; Schneider, M.; Reich, M.-L.; Sommer, H.; Adelhelm, P.; Janek, J., Dynamic Formation of a Solid-liquid Electrolyte Interphase and its Consequences for Hybrid-battery Concepts. *Nat. Chem.* **2016,** *8* (5), 426-434.
14. Schleutker, M.; Bahner, J.; Tsai, C.-L.; Stolten, D.; Korte, C., On the Interfacial Charge Transfer between Solid and Liquid Li^+ Electrolytes. *Phys. Chem. Chem. Phys.* **2017,** *19* (39), 26596-26605.
15. Matios, E.; Wang, H.; Luo, J.; Zhang, Y.; Wang, C.; Lu, X.; Hu, X.; Xu, Y.; Li, W., Reactivity-guided Formulation of Composite Solid Polymer Electrolytes for Superior Sodium Metal Batteries. *J. Mater. Chem. A* **2021,** *9* (34), 18632-18643.
16. Yu, X.; Xue, L.; Goodenough, J. B.; Manthiram, A., A High-Performance All-Solid-State Sodium Battery with a Poly(ethylene oxide)–$Na_3Zr_2Si_2PO_{12}$ Composite Electrolyte. *ACS Mater. Lett.* **2019,** *1* (1), 132-138.
17. Yu, X.; Xue, L.; Goodenough, J. B.; Manthiram, A., Ambient-Temperature All-Solid-State Sodium Batteries with a Laminated Composite Electrolyte. *Adv. Funct. Mater.* **2021,** *31* (2), 2002144.
18. Jaschin, P. W.; Tang, C. R.; Wachsman, E. D., High-rate Cycling in 3D Dual-doped NASICON Architectures Toward Room-temperature Sodium-metal-anode Solid-state Batteries. *Energy Environ. Sci.* **2024,** *17* (2), 727-737.

19. Ren, Y.; Hortance, N.; McBride, J.; Hatzell, K. B., Sodium–Sulfur Batteries Enabled by a Protected Inorganic/Organic Hybrid Solid Electrolyte. *ACS Energy Letters* **2021,** *6* (2), 345-353.
20. Lim, Y. J.; Han, J.; Kim, H. W.; Choi, Y.; Lee, E.; Kim, Y., An Epoxy-reinforced Ceramic Sheet as a Durable Solid Electrolyte for Solid State Na-ion Batteries. *J. Mater. Chem. A* **2020,** *8* (29), 14528-14537.
21. Wang, C.; Yu, R.; Duan, H.; Lu, Q.; Li, Q.; Adair, K. R.; Bao, D.; Liu, Y.; Yang, R.; Wang, J.; Zhao, S.; Huang, H.; Sun, X., Solvent-Free Approach for Interweaving Freestanding and Ultrathin Inorganic Solid Electrolyte Membranes. *ACS Energy Lett.* **2022,** *7* (1), 410-416.
22. Shen, L.; Deng, S.; Jiang, R.; Liu, G.; Yang, J.; Yao, X., Flexible Composite Solid Electrolyte with 80 wt% $Na_{3.4}Zr_{1.9}Zn_{0.1}Si_{2.2}P_{0.8}O_{12}$ for Solid-state Sodium Batteries. *Energy Storage Mater.* **2022,** *46*, 175-181.
23. Luo, J.; Sun, Q.; Liang, J.; Adair, K.; Zhao, F.; Deng, S.; Zhao, Y.; Li, R.; Huang, H.; Yang, R.; Zhao, S.; Wang, J.; Sun, X., Rapidly In Situ Cross-Linked Poly(butylene oxide) Electrolyte Interface Enabling Halide-Based All-Solid-State Lithium Metal Batteries. *ACS Energy Lett.* **2023,** *8* (9), 3676-3684.
24. Jung, S.-K.; Gwon, H.; Yoon, G.; Miara, L. J.; Lacivita, V.; Kim, J.-S., Pliable Lithium Superionic Conductor for All-Solid-State Batteries. *ACS Energy Lett.* **2021,** *6* (5), 2006-2015.
25. Wen, F.; Xie, G.; Chen, N.; Wu, Q.; Chaudhary, M.; You, X.; Michaelis, V. K.; Mar, A.; Sang, L., Mechanochemistry in Sodium Thioantimonate Solid Electrolytes: Effects on Structure, Morphology, and Electrochemical Performance. *ACS Applied Materials & Interfaces* **2023,** *15* (33), 40070-40079.
26. Famprikis, T.; Kudu, Ö. U.; Dawson, J. A.; Canepa, P.; Fauth, F.; Suard, E.; Zbiri, M.; Dambournet, D.; Borkiewicz, O. J.; Bouyanfif, H.; Emge, S. P.; Cretu, S.; Chotard, J.-N.; Grey, C. P.; Zeier, W. G.; Islam, M. S.; Masquelier, C., Under Pressure: Mechanochemical Effects on Structure and Ion Conduction in the Sodium-Ion Solid Electrolyte Na3PS4. *Journal of the American Chemical Society* **2020,** *142* (43), 18422-18436.
27. Maus, O.; Agne, M. T.; Fuchs, T.; Till, P. S.; Wankmiller, B.; Gerdes, J. M.; Sharma, R.; Heere, M.; Jalarvo, N.; Yaffe, O.; Hansen, M. R.; Zeier, W. G., On the Discrepancy between Local and Average Structure in the Fast Na+ Ionic Conductor Na2.9Sb0.9W0.1S4. *Journal of the American Chemical Society* **2023,** *145* (13), 7147-7158.
28. Karmakar, A.; Dodd, M. S.; Agnihotri, S.; Ravera, E.; Michaelis, V. K., Cu(II)-Doped Cs2SbAgCl6 Double Perovskite: A Lead-Free, Low-Bandgap Material. *Chemistry of Materials* **2018,** *30* (22), 8280-8290.
29. Kalisvaart, W. P.; Chaudhary, M.; Bhattacharya, A.; Michaelis, V. K.; Buriak, J. M., Mixing, Domains, and Fast Li-Ion Dynamics in Ternary Li–Sb–Bi Battery Anode Alloys. *The Journal of Physical Chemistry C* **2022,** *126* (5), 2394-2402.
30. Krauskopf, T.; Culver, S. P.; Zeier, W. G., Local Tetragonal Structure of the Cubic Superionic Conductor Na3PS4. *Inorganic Chemistry* **2018,** *57* (8), 4739-4744.
31. Sivakumar, M.; Dasgupta, A.; Ghosh, C.; Sornadurai, D.; Saroja, S., Optimisation of high energy ball milling parameters to synthesize oxide dispersion

strengthened Alloy 617 powder and its characterization. *Advanced Powder Technology* **2019,** *30* (10), 2320-2329.
32. Chaudhary, M.; Pominov, A.; Mumbaraddi, D.; Allen, B.; Meyer, J.; Kirchberger, A. M.; Bernard, G. M.; Nilges, T.; Mar, A.; Michaelis, V. K., Drop That Activation Energy: Tetragonal to Cubic Transformations in Na3PS4−xSex for Solid State Sodium Ion Battery Materials. *Advanced Functional Materials n/a* (n/a), 2311829.
33. Xie, G.; Tang, M.; Xu, S.; Brown, A.; Sang, L., Degradation at the Na3SbS4/Anode Interface in an Operating All-Solid-State Sodium Battery. *ACS Applied Materials & Interfaces* **2022,** *14* (43), 48705-48714.
34. Cuba-Chiem, L. T.; Huynh, L.; Ralston, J.; Beattie, D. A., In Situ Particle Film ATR FTIR Spectroscopy of Carboxymethyl Cellulose Adsorption on Talc: Binding Mechanism, pH Effects, and Adsorption Kinetics. *Langmuir* **2008,** *24* (15), 8036-8044.
35. Max, J.-J.; Chapados, C., Infrared Spectroscopy of Aqueous Carboxylic Acids: Comparison between Different Acids and Their Salts. *The Journal of Physical Chemistry A* **2004,** *108* (16), 3324-3337.
36. Max, J.-J.; Chapados, C., Infrared Spectroscopy of Aqueous Carboxylic Acids: Malic Acid. *The Journal of Physical Chemistry A* **2002,** *106* (27), 6452-6461.
37. Vasko, P. D.; Blackwell, J.; Koenig, J. L., Infrared and raman spectroscopy of carbohydrates.: Part II: Normal coordinate analysis of α-D-glucose. *Carbohydrate Research* **1972,** *23* (3), 407-416.
38. Joshi, S.; Kalyanasundaram, S.; Balasubramanian, V., Quantitative Analysis of Sodium Carbonate and Sodium Bicarbonate in Solid Mixtures Using Fourier Transform Infrared Spectroscopy (FT-IR). *Appl. Spectrosc.* **2013,** *67* (8), 841-845.
39. Cuba-Chiem, L. T.; Huynh, L.; Ralston, J.; Beattie, D. A., In situ particle film ATR-FTIR studies of CMC adsorption on talc: The effect of ionic strength and multivalent metal ions. *Minerals Engineering* **2008,** *21* (12), 1013-1019.
40. Cael, J. J.; Koenig, J. L.; Blackwell, J., Infrared and raman spectroscopy of carbohydrates: Part IV. Identification of configuration- and conformation-sensitive modes for D-glucose by normal coordinate analysis. *Carbohydrate Research* **1974,** *32* (1), 79-91.
41. Zhang, Y.; Lu, W.; Zhao, P.; Aboonasr Shiraz, M. H.; Manaig, D.; Freschi, D. J.; Liu, Y.; Liu, J., A durable lithium–tellurium battery: Effects of carbon pore structure and tellurium content. *Carbon* **2021,** *173*, 11-21.
42. Wang, H.; Tong, Z.; Yang, R.; Huang, Z.; Shen, D.; Jiao, T.; Cui, X.; Zhang, W.; Jiang, Y.; Lee, C.-S., Electrochemically Stable Sodium Metal-Tellurium/Carbon Nanorods Batteries. *Advanced Energy Materials* **2019,** *9* (48), 1903046.
43. Zhang, J.; Yin, Y.-X.; You, Y.; Yan, Y.; Guo, Y.-G., A High-Capacity Tellurium@Carbon Anode Material for Lithium-Ion Batteries. *Energy Technology* **2014,** *2* (9-10), 757-762.
44. Zhang, Y.; Liu, C.; Wu, Z.; Manaig, D.; Freschi, D. J.; Wang, Z.; Liu, J., Enhanced Potassium Storage Performance for K-Te Batteries via Electrode Design and Electrolyte Salt Chemistry. *ACS Applied Materials & Interfaces* **2021,** *13* (14), 16345-16354.
45. Kim, T. W.; Park, K. H.; Choi, Y. E.; Lee, J. Y.; Jung, Y. S., Aqueous-solution Synthesis of Na_3SbS_4 Solid Electrolytes for All-solid-state Na-ion Batteries. *J. Mater. Chem. A* **2018,** *6* (3), 840-844.

46. Zhang, Y.; Manaig, D.; Freschi, D. J.; Liu, J., Materials design and fundamental understanding of tellurium-based electrochemistry for rechargeable batteries. *Energy Storage Materials* **2021,** *40*, 166-188.
47. Flaman, G. T.; Boyle, N. D.; Vermelle, C.; Morhart, T. A.; Ramaswami, B.; Read, S.; Rosendahl, S. M.; Wells, G.; Newman, L. P.; Atkinson, N.; Achenbach, S.; Burgess, I. J., Chemical Imaging of Mass Transport Near the No-Slip Interface of a Microfluidic Device using Attenuated Total Reflection–Fourier Transform Infrared Spectroscopy. *Analytical Chemistry* **2023,** *95* (11), 4940-4949.
48. Morhart, T. A.; Read, S.; Wells, G.; Jacobs, M.; Rosendahl, S. M.; Achenbach, S.; Burgess, I. J., Attenuated Total Reflection Fourier Transform Infrared (ATR FT-IR) Spectromicroscopy Using Synchrotron Radiation and Micromachined Silicon Wafers for Microfluidic Applications. *Appl. Spectrosc.* **2018,** *72* (12), 1781-1789.
49. Morhart, T. A.; Read, S. T.; Wells, G.; Jacobs, M.; Rosendahl, S. M.; Achenbach, S.; Burgess, I. J., Micromachined multigroove silicon ATR FT-IR internal reflection elements for chemical imaging of microfluidic devices. *Analytical Methods* **2019,** *11* (45), 5776-5783.